A self-adaptive metamaterial beam with digitally controlled resonators for subwavelength broadband flexural wave attenuation

IOP Publishing Smart Materials and Structures
Smart Mater. Struct. 27 (2018) 045015 (13pp) https://doi.org/10.1088/1361-665X/aab167

A self-adaptive metamaterial beam with digitally controlled resonators for subwavelength broadband flexural wave attenuation

Xiaopeng Li[1], Yangyang Chen[1,3], Gengkai Hu[2] and Guoliang Huang[1,3]

[1] Department of Mechanical & Aerospace Engineering, University of Missouri, Columbia, MO, 65211, United States of America
[2] School of Aerospace Engineering, Beijing Institute of Technology, Beijing, 100081, People's Republic of China

E-mail: yc896@mail.missouri.edu and huangg@missouri.edu

Received 28 November 2017, revised 8 February 2018
Accepted for publication 22 February 2018
Published 14 March 2018

Abstract

Designing lightweight materials and/or structures for broadband low-frequency noise/vibration mitigation is an issue of fundamental importance both practically and theoretically. In this paper, by leveraging the concept of frequency-dependent effective stiffness control, we numerically and experimentally demonstrate, for the first time, a self-adaptive metamaterial beam with digital circuit controlled mechanical resonators for strong and broadband flexural wave attenuation at subwavelength scales. The digital controllers that are capable of feedback control of piezoelectric shunts are integrated into mechanical resonators in the metamaterial, and the transfer function is semi-analytically determined to realize an effective bending stiffness in a quadratic function of the wave frequency for adaptive band gaps. The digital as well as analog control circuits as the backbone of the system are experimentally realized with the guarantee stability of the whole electromechanical system in whole frequency regions, which is the most challenging problem so far. Our experimental results are in good agreement with numerical predictions and demonstrate the strong wave attenuation in almost a three times larger frequency region over the bandwidth of a passive metamaterial. The proposed metamaterial could be applied in a range of applications in the design of elastic wave control devices.

Keywords: adaptive metamaterial beam, digital control, subwavelength broadband wave attenuation

(Some figures may appear in colour only in the online journal)

1. Introduction

To find a material or structure with strong noise/vibration attenuation at broadband low-frequencies with minimal increase in weight has been regarded as the primary goal in the past in both material science and structural engineering. Recently, locally resonant acoustic/elastic metamaterials have attracted a great deal of attention due to their strong wave mitigation ability at low-frequencies [1–16]. The material approach based on the local resonance mechanism opens a new avenue in wave/vibration attenuation at subwavelength scales with applications including, but not limited to, noise treatment [5–9], underwater sound control [10–12], structural vibration [13, 14, 17–23] and earthquake engineering [24–26]. However, the resonant stopbands of elastic metamaterials are usually narrow in nature [9], which significantly limits their practical applications under broadband dynamic loads. To address this problem, a lot of research efforts have been proposed by integrating multiple resonators [21–23],

[3] Authors to whom any correspondence should be addressed.

adding highly dissipative materials [27, 28], and including materials with nonlinear properties [29–31]. Nonetheless, in real-world environments, these methods are still extremely difficult for extending their low frequency wave mitigation abilities enough to reach various frequency domains as needed.

Active/adaptive elastic metamaterials where smart materials are integrated into to the passive metamaterials, on the other hand, provide a flexible platform for tunable effective material properties and therefore tunable and/or adaptive vibration/wave attenuation [32–41]. The piezoelectric shunt technique has compelling advantages in adaptive metamaterial applications compared with other smart materials and structures, due to their quick response, easy implementation and light weight [32–47]. Different piezoelectric shunts have been developed based on resonant and negative capacitance analog circuits for tunable [32–35] and broadband vibration/wave attenuation [36–39], respectively. However, the two strategies have suffered from their own limitations. For the electrical resonant circuits, their attenuation occupies very narrow frequency ranges [37]. The negative capacitance circuits can produce broadband attenuation but they are very weak due to the limitation of circuit instabilities for realizing a negative capacitance value close to that of the piezoelectric material [38]. To address these limitations, many efforts have been conducted to suggest different shunting-based metamaterials by using circuits with gradient resonant frequencies [40], amplifier-resonator or resonator-amplifier feedback circuits [41, 42], digital multiple resonance circuits [43] and hybrid circuits [44, 45]. Furthermore, a relatively broadband and tunable wave attenuation has been successfully observed to some extent [43, 44]. It should be mentioned that the intensity or magnitude of vibration/wave attenuation due to shunting circuits in structures with only piezoelectric patches attached is much weaker than that produced by the metamaterials with mechanical resonators because the mechanical wave energy dissipation induced by the electric boundary is very limited. Moreover, a method to enhance the dissipation performance from the electric boundary has not been fully solved thus far. With this consideration, an adaptive elastic metamaterial with tunable mechanical resonators was suggested by integrating tunable or adaptive stiffness elements into the mechanical local resonators [37], and therefore, the wave attenuation ability of the adaptive metamaterial can be tuned or adapted electronically and is also strong because it is based on tunable mechanical resonators. Based on this concept, Zhu *et al* [46] designed an adaptive elastic metamaterial where harmonic vibration as well as transient wave propagation tests were conducted to illustrate their tunable vibration suppression and elastic wave attenuation abilities. More recently, by integrating hybrid-circuit-shunted piezoelectric stacks with self-adaptive frequency-dependent stiffness into the resonant microstructures, high- and low-pass filtering capabilities of an adaptive metamaterial were demonstrated both analytically and numerically at subwavelength scales [47]. However, the conceptual design [46] requires the prior knowledge of the frequency information of the incident wave to perform active control, and the tuned band gaps are still narrow in real time. In addition, the experimental demonstration of the self-adaptive metamaterial for broadband wave attenuation is very scarce due to the difficulty of finding simple and implementable electric circuits to adaptively control effective material properties in real time.

In this study, we propose a new design of the self-adaptive metamaterial comprised of local resonant cantilever beams with piezoelectric sensors and actuators connected by digital circuits as feedback control loops for frequency-dependent effective bending stiffness control and, for the first time, experimentally demonstrate strong broadband flexural wave attenuation at a deep subwavelength scale. We establish a novel theoretical framework, which has never been explored before, to establish the relationship between the transfer function of the circuit system and the frequency-dependent effective bending stiffness. An analytical form of the transfer function is derived. The design is validated by three-dimensional piezoelectric coupled numerical simulations, where the transfer function is determined based on wave dispersion analyses. Extremely broadband low-frequency (unit cells are at subwavelength scales) flexural wave attenuation is obtained numerically that coincides with the analytical predictions. By considering electro-mechanical system stabilities in different frequency regions, the digital control system is then physically built with the transfer function coded into the micro-controller for easy implementation and tuning in contrast of pure analog circuits. Our experimental results demonstrate that the strong wave attenuation region can be self-adapted and extended to much lower frequency ranges compared with the passive metamaterial. The strategy proposed make it an excellent candidate for the design of elastic wave control devices in general, and for broadband low-frequency mechanical response control in particular.

2. Theoretical modeling of the self-adaptive metamaterial

Figure 1(a) shows the schematic of the adaptive metamaterial beam with the lattice constant, L, width, w_h, and thickness, h, for broadband low-frequency wave mitigation. The metamaterial unit cell is constructed by cutting a 'U' shaped thin slot with the width denoted by w_s out of the host beam to form a locally resonant cantilever beam located in the center of the unit cell. The width and length of the cantilever beam are denoted as w_b and l_b, respectively. To generate low-frequency locally resonant band gaps, two proof masses are attached on the tip of the cantilever beam symmetrically to its mid-plane with the length, width and height being l_m, w_m and h_m, respectively. Two piezoelectric patches are then surface bonded adjacent to the other end of this beam with l_p, w_p and h_p representing the length, width and thickness of each of the patches, respectively. To achieve the frequency-dependent effective bending stiffness control, a feedback control loop is applied [42] (figure 1(a)). The piezoelectric patch on one side of the cantilever beam functions as a sensor, and the piezoelectric patch on the other side of this beam acts as an actuator. A shunting circuit is then designed to connect the sensor and the actuator. Specifically, a charge amplifier with a reference capacitance C_1 is implemented to convert the sensing current from the sensor to an input voltage signal for this shunting circuit. A digital micro-controller coded

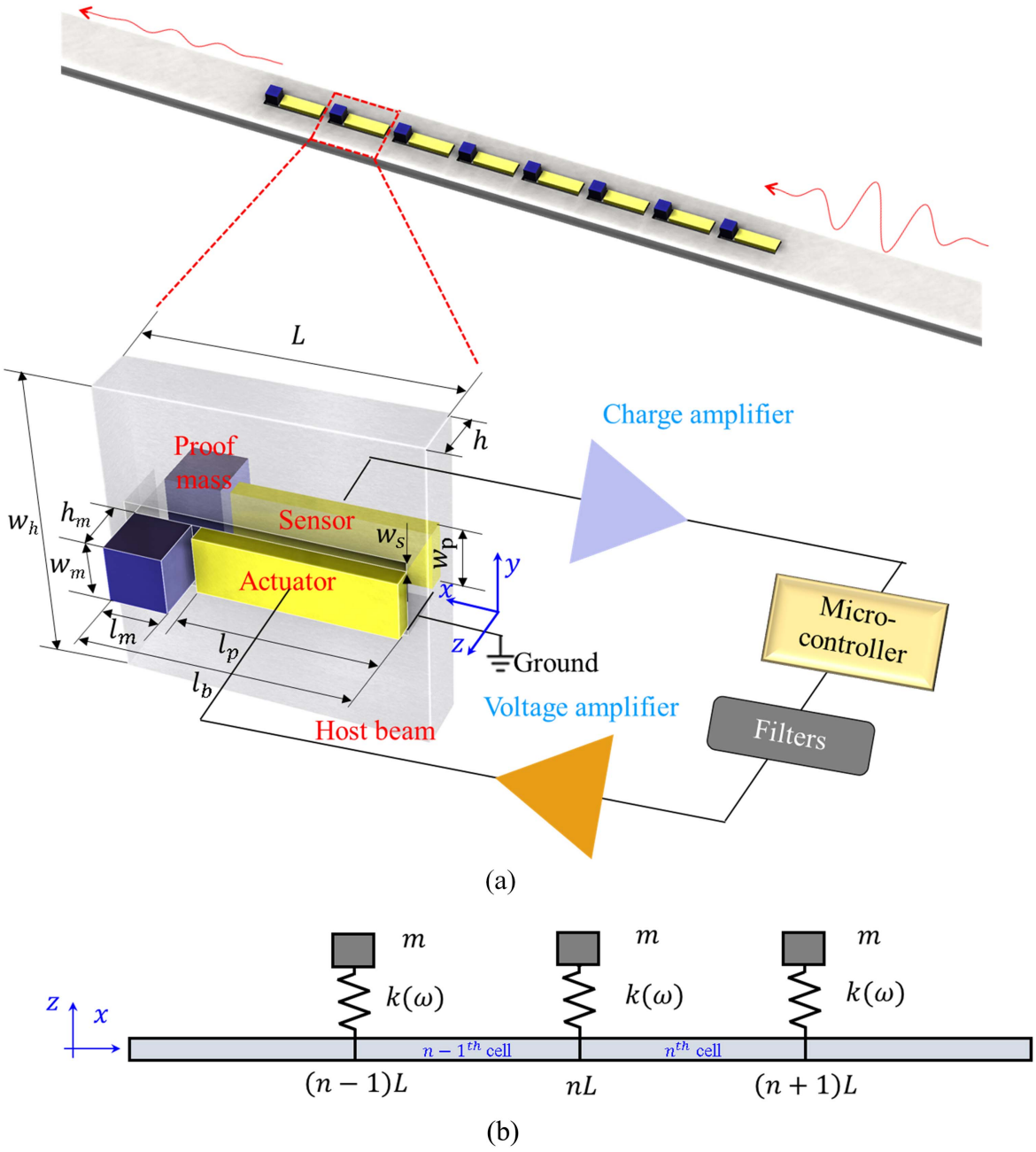

Figure 1. (a) Schematic of the adaptive metamaterial beam; (b) Schematic of the simplified 2D analytical model of the adaptive metamaterial beam.

with a transfer function calculates an output signal for actuating based on the input sensing signal. A proportional circuit is used to amplify this output voltage and apply it to the actuator. At the same time, this actuation also induces an extra sensing signal due to the electromechanical coupling, which in turn constitutes a local feedback control loop. It is worth mentioning that some necessary filters (such as low-pass, high-pass, and band-stop filters) are implemented to stabilize the feedback system, which will be discussed in the experimental testing section. To conduct the analytical analysis, the adaptive metamaterial beam is represented by a simplified model as shown in figure 1(b), where the periodic adaptive cantilever beam resonators are simplified by an array of mass-spring resonators attached to the host beam in which the mass, m, represents the equivalent tip masses and the spring constants,

$$k(\omega) = 3D_{eff}(\omega)/{l_b}^3, \tag{1}$$

where D_{eff} represents the effective bending stiffness of the piezoelectric cantilever beam.

2.1. Determination of the transfer function of the circuit system

Circuit transfer functions, governing the feedback behavior in the electrical domain, play the central role in the effective bending stiffness control of the cantilever beam. In the

following sections, two-step studies are performed to determine the transfer function of the adaptive resonator. First, the band gap edge frequencies of the simplified model with different frequency-independent spring constants will be analytically estimated, and we then characterize an effective bending stiffness of the cantilever beam as a quadratic function of the frequency to produce broadband wave attenuation. In the second step, we develop an analytical model to illuminate the relationship between the effective bending stiffness and the transfer function to finalize the design.

For the simplified model (figure 1(b)), the equation of motion of the host beam can be expressed, according to the Timoshenko beam hypotheses, as [47]

$$\frac{E_b I_b}{\rho_b S_b}\frac{\partial^4 w}{\partial x^4} - \frac{I_b}{S_b}\left(1 + \frac{E_b}{\kappa_b G_b}\right)\frac{\partial^4 w}{\partial x^2 \partial t^2} + \frac{\partial^2 w}{\partial t^2} + \frac{\rho_b I_b}{\kappa_b G_b S_b}\frac{\partial^4 w}{\partial t^4} = 0 \tag{2}$$

where w represents the out-of-plane displacement on the centroidal axis of the host beam, and E_b, G_b, ρ_b, I_b, S_b, and κ_b denote the Young's modulus, shear modulus, mass density, area moment of inertia, area of the cross-section and Timoshenko shear coefficient of the host beam, respectively. A harmonic solution to equation (2), $w(x,t) = W(x)e^{i\omega t}$, is considered and the harmonic time terms are dropped in the following equations. The effect of the resonators to the host beam can be represented by point forces from the spring connections. For the nth unit cell, the point force can be written as [22, 23, 47]

$$F_n = -\frac{mk\omega^2}{k - m\omega^2} W_n(nL), \tag{3}$$

where $W_n(x)$ denotes the out-of-plane wave field in the nth unit cell. By considering the Bloch theorem and combining the continuity conditions of the displacement, rotational angle of the cross-section, bending moment, and shear force at the point, $x = nL$, a generalized eigenvalue problem can be derived, from which the wave dispersion relations are obtained [22, 23, 47].

Figure 2 shows the contour of the imaginary part of the wavenumber for a periodic metamaterial beam with different frequency-independent effective stiffnesses, $k*$, where geometric and material parameters of the metamaterial beam are given in table 1. The mass denoted by m is calculated based on the geometry of the structure. The effective stiffness of the piezoelectric beam with short circuit is written as $k_0 = \frac{3}{l_b^3}\left(\frac{w_b E_b h^3}{12} + \frac{w_b(4h_p^3 + 6hh_p^2 + 3h^2h_p)}{6s_{11}^E}\right)$ with s_{11}^E being the compliance coefficient of the piezoelectric material under a constant electric field. The non-dimensionalized frequency, Ω, is defined as $\Omega = \frac{\omega}{\omega_0}$, where $\omega_0 = \sqrt{\frac{k_0}{m}}$. The color bar in the figure represents the wave attenuation along the x-direction [47], which implies that wave band gap frequencies exist in the entire colored region. Here, only low-frequency resonant band gaps are considered for the current study. As illustrated in the figure, the resonance gap occupies higher and broader frequency regions with a larger normalized stiffness,

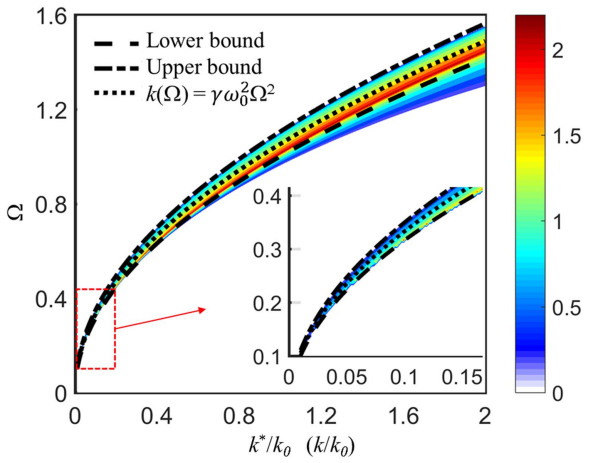

Figure 2. Normalized resonant band gap frequency region and estimated lower and upper band gap bound frequencies of the metamaterial beam with different frequency-independent normalized stiffness, $k*/k_0$, and selected frequency-dependent normalized stiffness, k/k_0, for broadband low-frequency wave attenuation.

and occupies lower and narrower regions with a smaller normalized stiffness [47]. Determining a stiffness in function of the frequency, $k(\omega)$, located within this band gap region, is the key for broadband wave attenuation. However, this determination cannot be easily accomplished in a fully analytical manner due to the complex boundary conditions.

On the other hand, the lower and upper bounds of the resonant band gaps can be approximately estimated as

$$\omega_l = \sqrt{\frac{k}{m}}, \tag{4a}$$

$$\omega_u = \sqrt{\frac{(m_h + m)}{m_h}}\sqrt{\frac{k}{m}}, \tag{4b}$$

where m_h represents the weight of the host beam, and the local deformation of the host beam is ignored due to the subwavelength dimensions. Based on equation (4), the lower and upper bounds are plotted as dashed and dash-dot curves in figure 2 in comparison with the exact solutions from the simplified model (shaded region). It can be found that the upper bound of the band gaps follows almost exactly to the simplified model, however, for the approximated lower bound, there exists some discrepancies when the normalized stiffness is greater than 0.5, which are caused by the low-frequency Bragg scattering at subwavelength scales [45] that the estimation cannot capture. It is noticed that if the frequency-dependent stiffness is designed to follow the estimated lower bound of the band gaps, $k(\omega) = m\omega^2$, the final wave attenuation region will cover the whole frequency region of the resonant band gaps shown in figure 2. Inspired by this observation, the effective stiffness could be assumed in a quadratic function of the frequency as,

$$k(\omega) = \gamma\omega^2, \text{ with } m \leqslant \gamma \leqslant m_h m/(m_h + m). \tag{5}$$

where γ is an arbitrary constant to be selected. As a validation, we select $\gamma = (m + m_h m/(m_h + m))/2$ and the corresponding effective stiffness curve (dotted curve) is added

Table 1. Geometric and material parameters of the proposed adaptive metamaterial beam.

Geometric parameters (mm)					
L	16.0	w	16.0	h	3.0
l_b	13.5	w_b	3.0	w_s	0.5
l_p	10.0	w_p	3.0	h_p	1.0
l_m	3.0	w_m	3.0	h_m	6.0
Material properties (Steel)					
E_b	210.0 GPa	G_b	80.8 GPa	ρ_b	7800.0 kg m^{-3}
Material properties (APC 850)					
s_{11}^E		16.4×10^{-12} m^2 N^{-1}	d_{33}		374.0×10^{-12} C N^{-1}
s_{33}^E		18.8×10^{-12} m^2 N^{-1}	d_{31}		-171.0×10^{-12} C N^{-1}
s_{44}^E		47.5×10^{-12} m^2 N^{-1}	d_{15}		584.0×10^{-12} C N^{-1}
s_{12}^E		-5.74×10^{-12} m^2 N^{-1}	ε_{33}^S		830.0 ε_0
s_{13}^E		-7.22×10^{-12} m^2 N^{-1}	ε_{11}^S		916.0 ε_0
ρ_p		7750.0 kg m^{-3}	ε_0		8.842×10^{-12} C mV^{-1}

in figure 2, where extremely broadband wave attenuation in the low-frequency range could be expected.

In the next study, we will analyze the adaptive metamaterial by quantitatively determining the relationship between the desired effective bending stiffness satisfying equation (5) and transfer functions in the electrical system through a multi-physical modeling. Here, the locally resonant cantilever beam is modeled based on the Kirchhoff hypotheses with the origin on the cantilever end. Because the actuating voltage is only applied across the actuator, the displacement field along the x-direction in the piezoelectric cantilever beam cannot be symmetric with respect to its mid-plane. As a result, we consider the displacement field along the x-direction as [45]

$$u(x, z) = -z\frac{\partial w}{\partial x} + u_0, \tag{6}$$

where u_0 represents the longitudinal displacement along the x-direction on the mid-plane of the beam. The corresponding normal strain along the x-direction can then be written as

$$S_x(x, z) = -z\kappa + \frac{\partial u_0}{\partial x}, \tag{7}$$

where $\kappa = \frac{\partial^2 w}{\partial x^2}$ denotes the curvature of the beam.

The linear constitutive vs of the piezoelectric material in the cantilever beam can be expressed as [45]

$$S_x = s_{11}^E T_x + d_{31} E_z, \tag{8a}$$

$$D_z = d_{31} T_x + \varepsilon_{33}^T E_z, \tag{8b}$$

where T_x, E_z, d_{31} and ε_{33}^T represent the normal stress along the x-direction, electric field along the z-direction, piezoelectric coupling coefficient and dielectric coefficient at constant stress, respectively. In general, the normal stresses on the cross-section of a beam are represented by a bending moment and a normal force with respect to the mid-plane of the beam, which can be calculated by performing corresponding integral operations over the entire thickness of the composite beam [45]. Integrating equation (8a), the bending moment can then be written as

$$M = D_p \kappa + A_b V_a, \tag{9}$$

where $D_P = \frac{w_b E_b h^3}{12} + \frac{w_b(4h_p^3 + 6hh_p^2 + 3h^2 h_p)}{6s_{11}^E}$ denotes the passive bending stiffness of the piezoelectric composite beam, $A_b = \frac{w_b d_{31}(h + h_p)}{2s_{11}^E}$, V_a represents the applied voltage on the actuating patch, and the electric field in the piezoelectric material is assumed as $E_z = -V_a/h$. Similarly, the normal force in the composite beam is expressed as

$$N = K_p \frac{\partial u_0}{\partial x} + A_N V_a, \tag{10}$$

in which $K_P = E_b h + \frac{2h_p}{s_{11}^E}$ and $A_N = \frac{d_{31}}{s_{11}^E}$. By assuming the proof mass as a lumped mass, the equation of longitudinal motion of the mass can be written as

$$N(x = l_p) = -\omega^2 m u_m, \tag{11}$$

where u_m denotes the displacement of the proof mass along the x-direction. For the cantilever beam operated at deep subwavelength scaled frequencies, we can assume $\frac{\partial u_0}{\partial x}$ uniform along the x-direction, which implies

$$u_m = l_p \frac{\partial u_0}{\partial x}. \tag{12}$$

Combining equations (10)–(12), we have

$$(-\omega^2 m l_p - K_p)\frac{\partial u_0}{\partial x} = A_N V_a. \tag{13}$$

At low-frequencies, $\omega^2 m l_p \ll K_p$, equation (13) can then be approximated as

$$\frac{\partial u_0}{\partial x} = -\frac{A_N}{K_p} V_a. \tag{14}$$

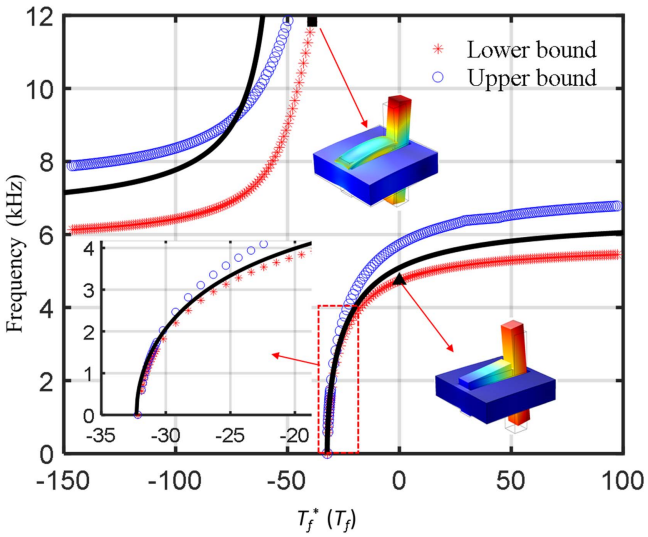

Figure 3. Numerically calculated upper (blue circles) and lower bound (red stars) frequencies of the resonant band gaps with different frequency-independent transfer functions, T_f^*, and the frequency-dependent transfer function, T_f, (black solid line) for broadband low-frequency wave attenuation.

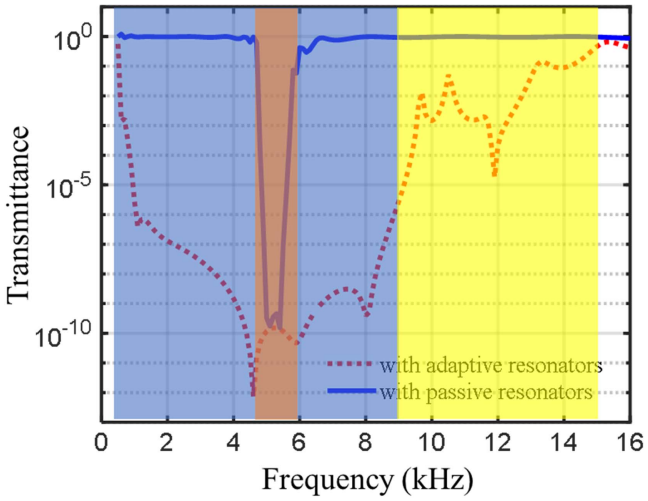

Figure 4. Numerically calculated wave transmittance of the metamaterial beam with eight unit cells with passive and adaptive resonators.

The charge amplifier in our design makes electrodes of the sensing patch virtually shorted. Thus, according to equation (8), the electrical displacement along the z-direction in the sensing piezoelectric material, D_z, is purely caused by the deformation of the patch, which is written as

$$D_z = s_b \kappa + s_L \frac{\partial u_0}{\partial x}, \tag{15}$$

where $s_b = -\frac{d_{31}\left(\frac{h}{2}+h_p\right)}{s_{11}^E}$ and $s_L = A_N$. By combining equations (14) and (15), the charge collected from the sensing electrode is

$$Q_s = \int_{S_p} -D_z ds = S_b \langle \kappa \rangle + S_L V_a, \tag{16}$$

where $S_b = -s_b l_p w_p$, $S_L = \frac{A_N}{K_p} s_L l_p w_p$ and $\langle \cdot \rangle$ denotes the average operation.

The input sensing voltage converted by the charge amplifier reads

$$V_s = -Q_s / C_1. \tag{17}$$

The relationship between the input sensing voltage and the output actuating voltage controlled by the transfer function is given as

$$T_f = \frac{V_a}{V_s}. \tag{18}$$

The effective bending stiffness of the piezoelectric beam is defined as

$$D_{eff} = \frac{\langle M \rangle}{\langle \kappa \rangle}. \tag{19}$$

By inserting equations (1), (5), (9), (16), (17) and (18) into equation (19), the transfer function is derived as

$$T_f = \frac{C_1(\gamma\omega^2 - D_p)}{A_b S_b - D_p S_L + \frac{3S_L\gamma\omega^2}{l_b^3}} = A_1 + \frac{A_3}{A_2 - \omega^2} \tag{20}$$

where $A_1 = C_1/S_L$, $A_2 = (D_p S_L - A_b S_b) \Big/ \left(\frac{3S_L\gamma\omega^2}{l_b^3}\right)$ and $A_3 = C_1 D_p/(S_L\gamma) - A_1 A_2$). Next, we will use numerical approaches to validate the broadband low-frequency wave attenuation of the adaptive metamaterial beam with this second order transfer function.

2.2. Numerical validations

Dispersion relations of flexural waves are calculated numerically based on the unit cell structure shown in figure 1(a) [47], by using a commercial finite element software, COMSOL Multiphysics. Geometric and material parameters of the adaptive metamaterial beam are listed in table 1 (around 5 unit cells within one wavelength at 4 kHz). Figure 3 shows the upper (blue circles) and lower bound frequencies (red stars) of the resonant band gaps from numerical wave dispersion calculations by prescribing different frequency-independent transfer functions as $T_f^* = \beta$, where β is an arbitrary constant and the reference capacitance in the charge amplifier is selected as $C_1 = 220$ pF. Different from the simplified analytical model in section 2.1, where only the fundamental mode of the cantilever beam is captured, the numerical simulation calculates both the fundamental and higher order modes. As shown in figure 3, two branches of resonant band gaps occupy low- and high-frequency regions, which are caused by the first- and second-order modes of the locally resonant cantilever beam, respectively (mode shapes are shown in the inset figures). As implied by the analytical model in section 2.1, frequency-independent transfer functions induce frequency-independent effective bending stiffness of the cantilever beam. Similar to those demonstrated in figure 2, by gradually decreasing β from zero to negative values, the lower and upper band gap bound frequencies are reduced and the band width becomes narrower for both the first- and second-order modes, due to the softening behavior

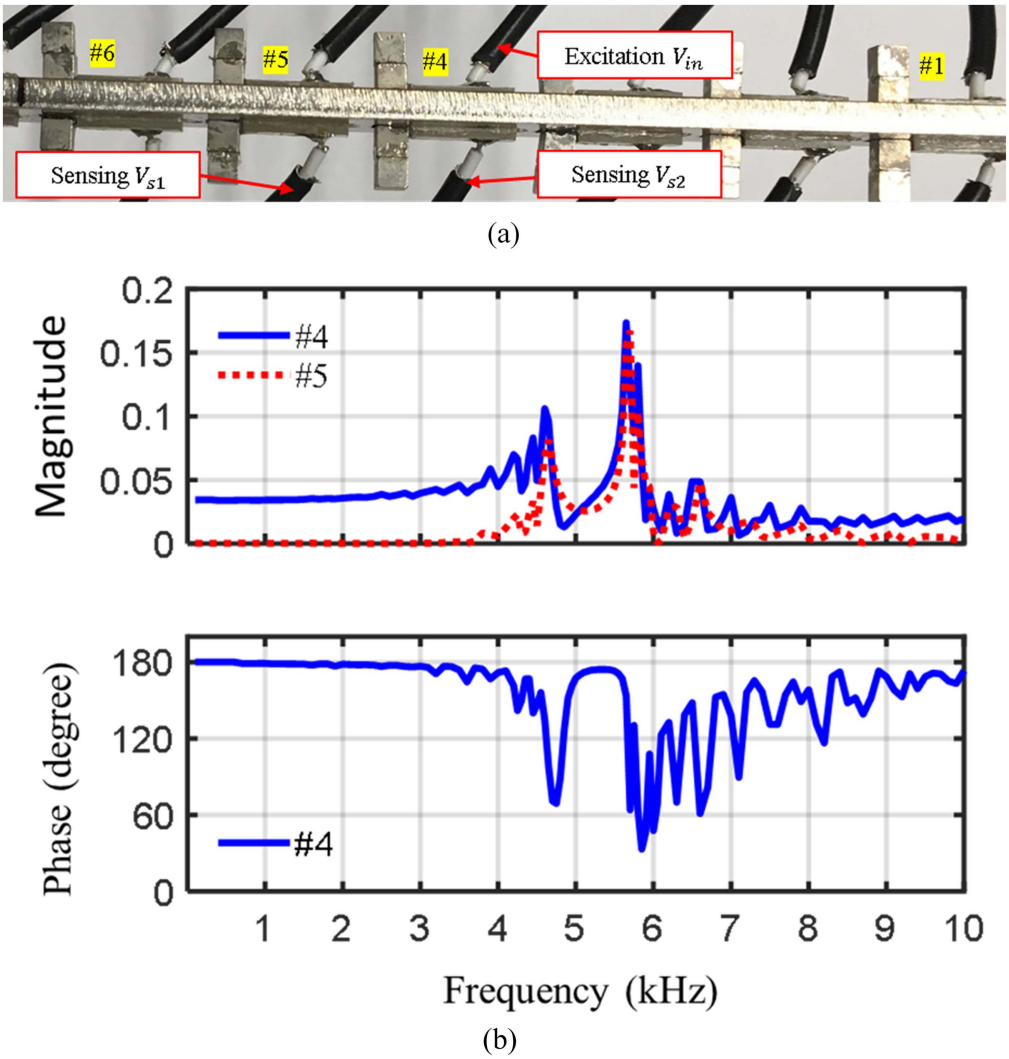

Figure 5. (a) Schematic of the experimental measurements of sensing voltages from the 4th and 5th unit cells of the metamaterial induced by the actuating voltage on the 4th unit cell; (b) Experimentally measured magnitude and phase angle of V_{s1}/V_{in} and V_{s2}/V_{in} at different frequencies.

caused by circuit feedback effects. On the other hand, by gradually increasing β from zero to positive values, the cantilever beam shows a hardening behavior, where both the lower and upper band gap bound frequencies are shifted and the band width becomes broader. It should be noted that the band gap tends to become convergent by further increasing β to extremely large values. Because, for those cases, the dominant deformation will be located at the host beam connected to the cantilever end, and the extremely high effective bending stiffness cannot contribute much to the change of the resonant frequency. Based on equation (20), the transfer function, $T_f = -52.62 + \frac{3.39 \times 10^{10}}{1.67 \times 10^9 - \omega^2}$ is selected and plotted in figure 3 (black curve) for the broadband wave mitigation. Some corrections of the constants in the transfer function are made due to inaccurate predictions of the simplified model, which come from the two main facts: (1) The simplified model is based on the plane stress assumptions. However, for a PZT material polarized along the z-direction, the piezoelectric effect is isotropic in the x-y plane, which violates those assumptions and would produce some differences; (2) In the real structure, the inner resonant cantilever beam is connected with the host beam directly, which is actually not a rigid connection. However, in the simplified model, we assumed a fix end of the inner resonant cantilever beam when calculating the effective bending stiffness, which also induces some errors. For this ideal case, when the transfer function $T_f(\omega)$ is located between the upper and lower bounds of the band gaps (derived with frequency-independent transfer function T_f^*), the band gap behavior of the adaptive metamaterial with the transfer function $T_f(\omega)$ will be activated at this frequency. Following this criterion, the band gap region of the adaptive metamaterial is from 0.5–9 kHz, indicating an extremely broadband wave attenuation region.

Figure 4 shows the numerical result of wave transmittance of the adaptive metamaterial beam with eight unit cells. For comparison, the wave transmittance in the passive metamaterial is included (blue solid curve), where the resonant attenuation region is observed from 4.6–6 kHz. By

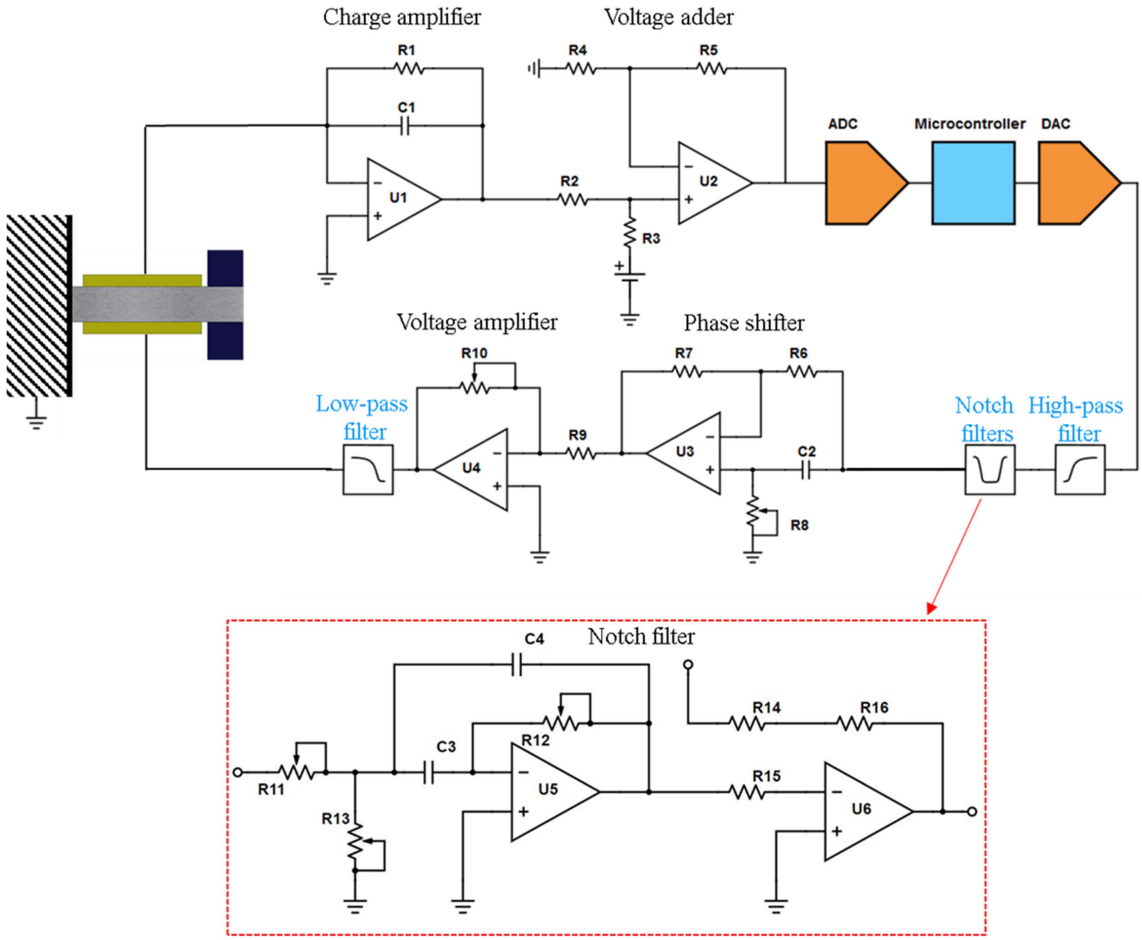

(a)

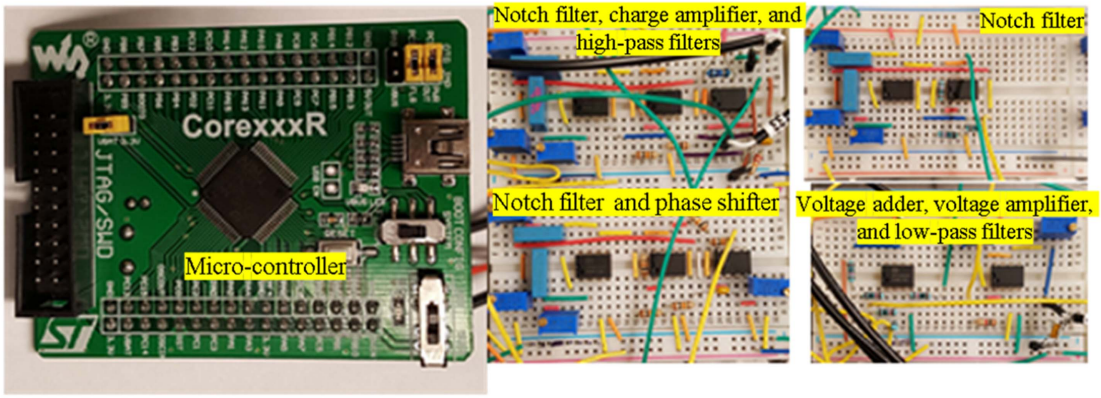

(b)

Figure 6. (a) Schematic of the circuit system of an adaptive metamaterial beam unit cell; (b) Photos of the micro-controller and fabricated analog circuits.

connecting the adaptive circuits to the metamaterial, the original wave attenuation region is enlarged to 0.5–15.0 kHz (red dashed curve), where the strong wave attenuation caused by the adaptive resonance occupies frequencies from 0.5 to 9.0 kHz (shade blue region), which coincides with the prediction in figure 3. The other weak wave attenuation region (9.0–15.0 kHz, shaded yellow) are attributed to the material mismatch due to the presence of the adaptive resonators.

3. Experimental validation of the adaptive metamaterial

3.1. Fabrication of the metamaterial structure

Based on the same material and geometric parameters as those in the numerical simulations, the adaptive metamaterial with eight unit cells is fabricated on a steel beam

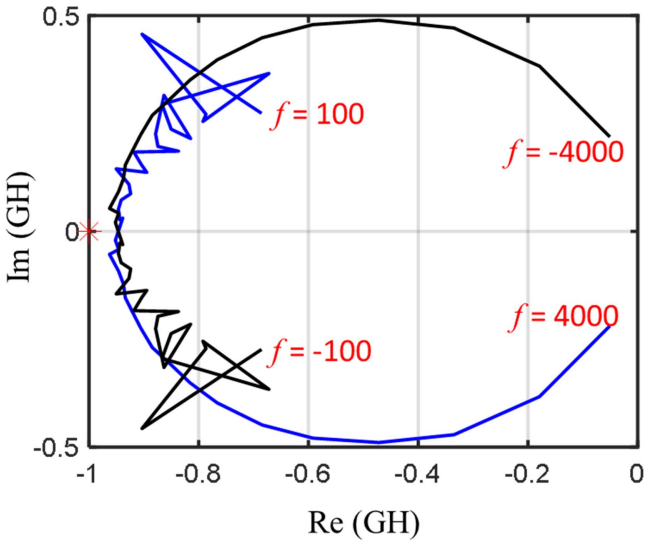

Figure 7. Nyquist plot of an adaptive metamaterial beam unit cell at frequencies below 4 kHz.

Table 2. Circuit parameters of the proposed adaptive metamaterial beam.

Component	Symbol	Value
Resistor	R_1	1 GW
	R_2-R_7, R_{14}-R_{16}	10 kW
	R_9	1 kW
Capacitor	C_1	220 pF
	C_2	100 nF
	C_3, C_4	10 nF
Op-amp	U_1-U_3, U_5, U_6	OPA604
	U_4	OPA445
Potentiometer	R_8	0–10 kΩ
	R_{10}	0–100 kΩ
	R_{11}, R_{12}	0–50 kΩ
	R_{13}	0–1 kΩ
Filters	High-pass filter $(RC)_{hp}$	3.5 kΩ × 100 nF
	Low-pass filter $(RC)_{lp}$	252.5 Ω × 102 nF

(1500 mm × 16 mm × 3 mm) for experimental testing. To fabricate the sample, we first cut an array of 'U' shaped thin slits out of the host beam with a micro-laser cutting machine to form the locally resonant cantilever beams. Two piezoelectric patches (APC 850, 10.0 mm × 3.0 mm × 1.0 mm) are bonded on both sides of the cantilever beams with a conductive epoxy. Steel masses with the total weigh being 0.8 g are attached on the tips of the cantilever beams with a commercially available superglue. The steel beam is grounded to function as an electric potential reference. Shielded cables are soldered on the electrodes of piezoelectric patches to insulate sensing and actuating signals.

3.2. Design of the circuit system

To implement the digital control circuits in the experiments, the stability of the electromechanical system must be considered as a priority. In general, the stability of a classical one-input/one-output feedback system can be quantified by the product of the loop transfer functions. In our design, the loop transfer functions comprise the transfer function of the electrical circuit (denoted by $G(\omega) = T_f(\omega)$, in the following) and the ratio between the sensing voltage (purely induced by the actuating voltage) and the actuating voltage controlled by the electromechanical coupling coefficient of the structure (denoted by $H(\omega)$).

The stability analysis starts from the function, $H(\omega)$. We first experimentally characterize the frequency range where the structure can be regarded as individual one-input/one-output feedback systems. Without loss of generality, a harmonic actuating voltage (V_{in}) is applied on one side of the piezoelectric patch of the 4th unit cell, and the sensing voltages (V_{s1} and V_{s2}) are acquired from charge amplifiers (with a 220 pF capacitor) from the other side of the piezoelectric patches of the 4th and the 5th unit cells of the metamaterial (figure 5(a)), respectively, to examine the responses within and between unit cells. Figure 5(b) shows the amplitude and phase angle of the sensing-actuating-voltage-ratios at different frequencies. For the 5th unit cell, the response is neglectable at the frequencies below 4 kHz, which indicates that the feedback control of the whole system can be decoupled between unit cells below 4 kHz, where the simple Nyquist plot would be enough to examine the stabilities. However, for the frequencies above 4 kHz, the coupling between unit cells is strong and cannot be ignored leading to a more complex stability analysis.

It can also be found from figure 5(b) that, for the 4th unit cell, both the amplitude and phase angle of $H(\omega)$ are nearly flat, as the frequency increases from 0 to 4 kHz, which implies that the electromechanical coupling coefficient is nearly uniform at these frequencies. In addition to this flat region, there also exists two strong peaks around 4.6 and 5.7 kHz, respectively. The first peak is caused by the local resonance of the cantilever beam, while the second peak is induced by the resonance of the periodic structure corresponding to the mode at $k_x = 0$. Around those two peaks, the phase angle experiences strong fluctuations. It is worth mentioning that the two peak frequencies coincide with the lower and upper bound frequencies of the resonant band gap in the passive metamaterial as our numerical simulation results shown in figure 3 for $T_f^* = 0$.

Next, we move our attention to the function, $G(\omega)$, to finalize the stability analysis. In practical circuit design, the ideal transfer function used in simulations needs to be modified first by including an imaginary frequency term into the denominator to avoid the pole at 6.5 kHz. This added term is determined by the maximum magnitude range of the voltage signals in the microcontrollers. By gradually increasing the added term, the response magnitude of the voltage signals can be reduced such that the signals in the microcontroller would not be over ranged and, at the same time, possess enough accuracies. In adaptive metamaterial applications, the added term is expected as small as possible to gain better wave attenuation performance at lower frequencies. By considering these two factors, the value of the added term is obtained. In the experiment, the transfer function is reformulated as

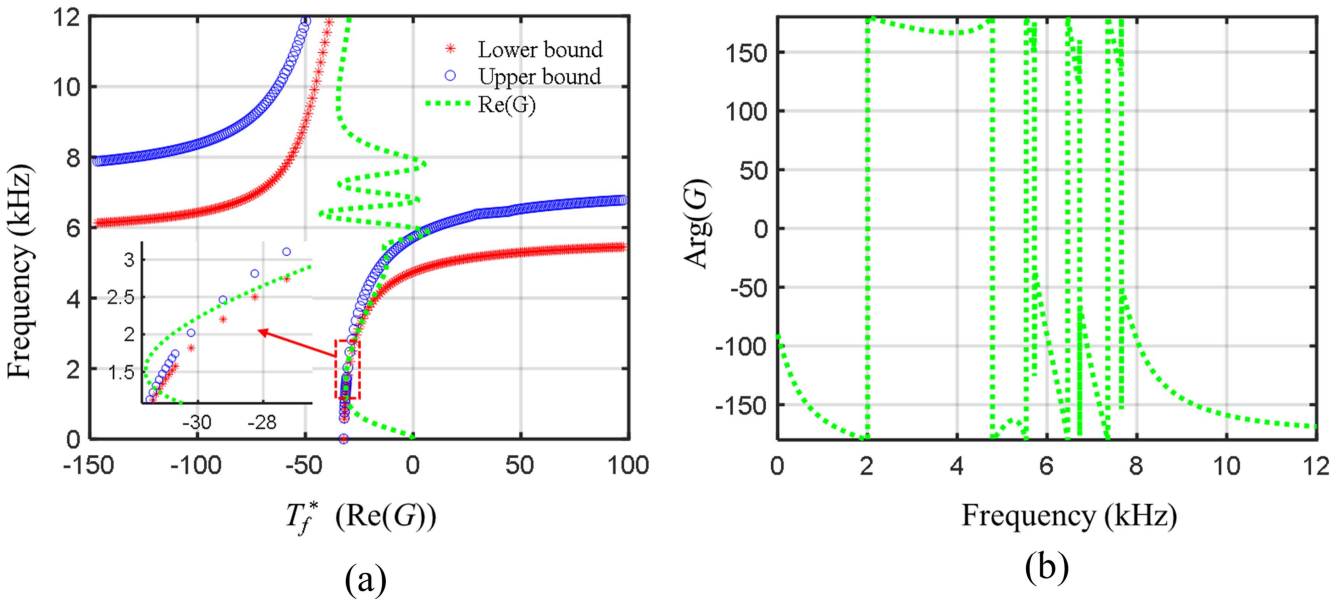

Figure 8. (a) Numerically calculated upper (blue circles) and lower bound (red stars) frequencies of the resonant band gaps with different frequency-independent transfer functions, T_f^*, and experimentally realized real part of the transfer function, Re(G), for broadband low-frequency wave attenuation; (b) Phase angle of the experimentally realized transfer function.

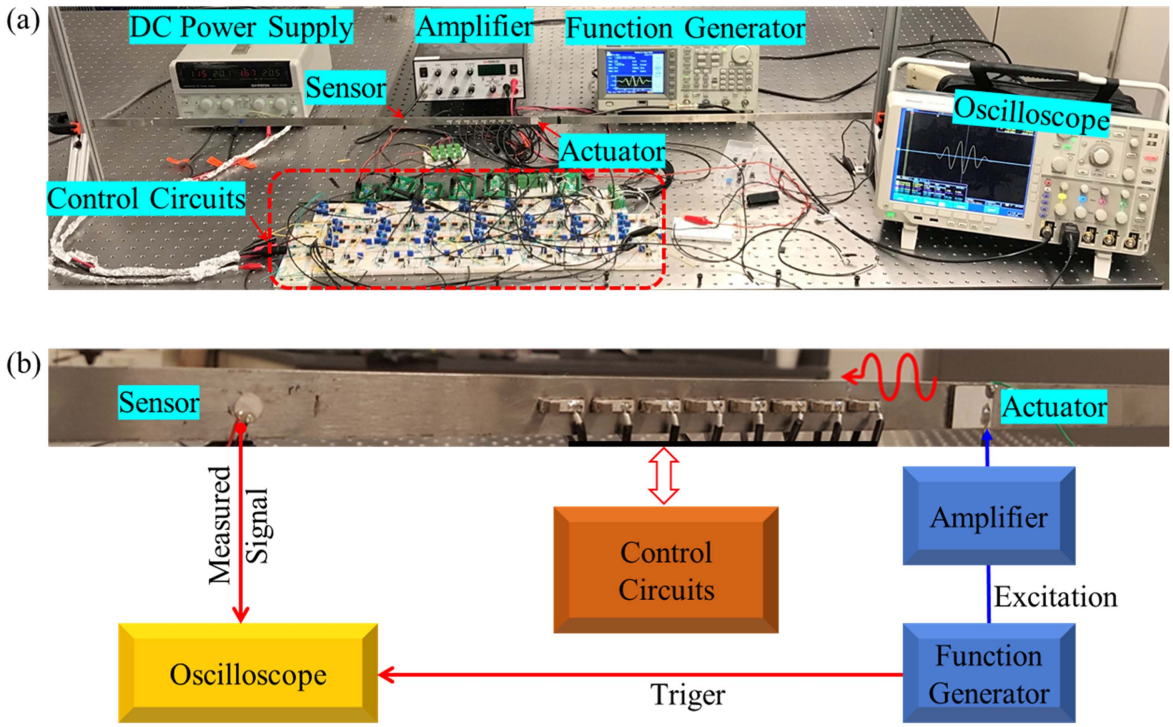

Figure 9. (a) Schematic of the experimental setup of the wave transmission test; (b) Detailed demonstration of connections between the testing equipment and fabricated adaptive metamaterial beam.

$T_f = -52.62 + \frac{3.39 \times 10^{10}}{1.67 \times 10^9 + 1100^*2 * \pi * i\omega - \omega^2}$, and aims to achieve the broadband low-frequency wave attenuations starting from 2 kHz. To realize this transfer function, a digital micro-controller (STM32F405) with a voltage amplifier is implemented (figure 6(a)), where the computational time delay of this second-order transfer function is calibrated as around 3 μs. A voltage adder and a first-order high-pass filter circuit with the cut-off frequency being 455 Hz are then connected to the digital controller for proper operations (figure 6(a)). To suppress high-frequency signal noises, a first-order low-pass filter with the cut-off frequency being 6.18 kHz is integrated. It should be mentioned that the low-pass filter also guarantees the stability at high-frequencies, where the circuit feedback effects are suppressed. A phase

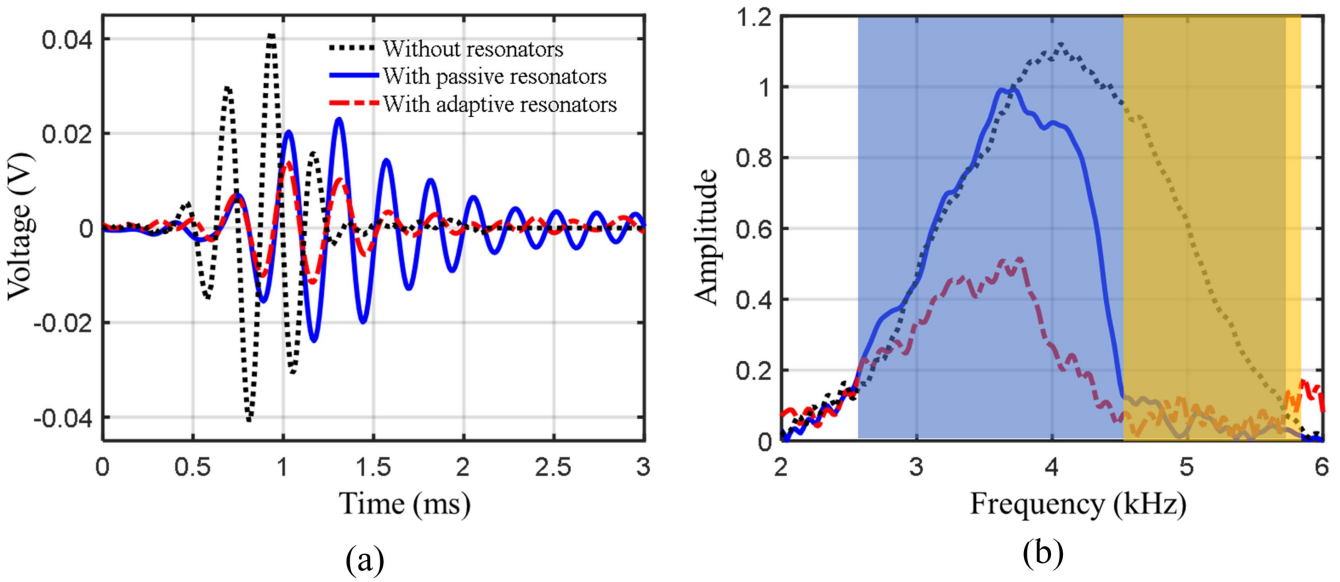

Figure 10. Experimentally measured (a) time-domain and (b) frequency-domain signals of transmitted waves with passive resonators, adaptive resonators and without resonators.

shifting circuit is also implemented to compensate for the phase delay caused by the microcontroller and the low-pass filter such that the phase of G can be tuned to π at 2.0 kHz.

With functions, H and G, the system stability is first examined by a Nyquist plot (figure 7) at low-frequencies ($f < 4$ kHz) for the 4th unit cell of the metamaterial. Other unit cells function in the same way and have similar results that will not be illustrated here for brevity. It can be seen from figure 7 that the two Nyquist curves do not encircle the point $(-1, 0)$ or interact with the real axis at the left-hand-side of this point, which implies that the system is quasi-stable below 4.0 kHz. For the frequencies above 18.0 kHz, the stability is guaranteed by the low-pass filter, which produce very strong signal suppression (<-10 dB). Thus, the unstable frequency points can only be located between 4.0–18.0 kHz.

Next, we examine those unstable frequencies through experimental testing, and implement some notch filters accordingly into the circuit to stabilize the electromechanical system. Notch filters are selected, because they produce minimum amplitude and phase changes at other unfiltered frequencies, which guarantees the performance of the transfer function designed at desired frequencies. By connecting the circuits without notch filters to a metamaterial unit cell, we find a divergent frequency around 5.7 kHz. This is understandable as H has a strong response near 5.7 kHz. Then, by adding a notch filter tuned at 5.7 kHz to the metamaterial unit cell circuit, another divergent frequency is found around 7.5 kHz, which is caused by the strong response of the transfer function. Therefore, another notch filter tuned at 7.5 kHz is added to make a metamaterial unit cell stable at entire frequencies. However, due to the strong coupling between metamaterial unit cells at frequencies between 4.0–8.0 kHz, an extra divergent frequency around 6.5 kHz is appeared when multiple metamaterial unit cells are connected with adaptive circuits. As a result, a third notch filter tuned at 6.5 kHz is implemented into the digital circuit system to make the whole system stable. It should be mentioned that all the notch filters are implemented with analog circuits, because digital filters produce significant time delays. All the circuit parameters are finalized and listed in table 2. The photograph of the fabricated circuit system is shown in figure 6(b).

Figure 8 shows the lower and upper bound frequencies of the resonant band gaps from numerical simulations and the transfer function of the circuit in the experiment to check the wave attenuation region in the design. It can be observed that the wave attenuation region from 2.3–5.7 kHz is obtained, where the real part of the real circuit transfer function is located in the band gap region and the phase angle is close to π.

3.3. Wave transmission testing

The schematic of the experimental setup for wave transmission testing is shown in figure 9. A piezoelectric plate (20 mm × 16 mm × 1.4 mm) is bonded 80 mm away from the metamaterial sample to generate incident flexural waves. Another piezoelectric disk with the diameter and thickness being 6.36 mm and 0.76 mm, respectively, is attached on the other side of the sample to detect the transmitted wave signal. In the experiment, a four-peak tone-burst signal with the center frequency, $f_c = 4$ kHz, is generated by a function generator (Tektronix AFG 3021) and amplified by a power amplifier (Krohn-Hite 7602 M) for the incident wave excitations. The wave mode induced by the actuator is primarily asymmetric mode at frequencies from 2.0–6.0 kHz [48]. The transmitted wave signals are acquired by a digital oscilloscope (Tektronix DPO4034).

Figure 10 shows the time- and frequency-domain signals of transmitted waves with metamaterials with open and adaptive circuits as well as without metamaterials. As the dotted black curve illustrates in the figure, the incident signal

contains very broadband frequency components (from 2 to 6 kHz). When the passive metamaterial is used, the amplitude of the transmitted wave can be reduced. The wave attenuation region is only located between 4.5 to 5.8 kHz, which agrees very well with our numerical results shown in figure 4. However, the wave attenuation provided by the passive metamaterial is insufficient for such a broadband signal. By using six adaptive metamaterial unit cells, the amplitude of the transmitted wave can be decreased further. The wave attenuation region from 2.5 to 5.7 kHz is clearly seen, which agrees well with the prediction in figure 8. It is also noticed that the wave mitigation ability of the adaptive metamaterial at lower frequencies (2.5–4.5 kHz) is not as strong as the passive metamaterial in the band gap frequency region (4.5–6.0 kHz), which is mainly caused by the added term in the transfer function of the microcontroller that will induce damping properties in the resonators. It should be mentioned that the similar experimental observation will be obtained by using eight unit cells. The wave attenuation region produced by the adaptive metamaterial enlarges the passive wave attenuation region by a factor of 2.46 without any increase in weight.

4. Conclusion

In the study, we, for the first time, numerically and experimentally demonstrate a self-adaptive metamaterial for strong broadband low-frequency wave attenuation with adaptive mechanical local resonators, by leveraging the concept of the frequency-dependent stiffness. The adaptive resonators are comprised of local resonant cantilever beams with piezoelectric sensors and actuators connected by digital circuits as feed-back control loops. Theoretical and numerical studies are systematically performed to determine the transfer functions of the electrical circuit system. The circuits are experimentally implemented by considering stabilities of the whole electromechanical system in different frequency regions. The experimental results demonstrate a strong wave attenuation region at low-frequencies which is 2.46 times larger compared with the band width of a passive metamaterial. The design could be extended to different length and time scales for much lower- or higher-frequency operations and immediately benefit a range of broadband low-frequency vibration/wave attenuation applications.

Acknowledgments

This work is supported by the Air Force Office of Scientific Research under Grant No. AF 9550-15-1-0016 with Program Manager Dr Byung-Lip (Les) Lee.

ORCID iDs

Guoliang Huang https://orcid.org/0000-0003-0959-8427

References

[1] Liu Z, Zhang X, Mao Y, Zhu Y Y, Yang Z, Chan C T and Sheng P 2000 Locally resonant sonic materials *Science* **289** 1734–6
[2] Ma G and Sheng P 2016 Acoustic metamaterials: from local resonances to broad horizons *Sci. Adv.* **2** e1501595
[3] Huang H H, Sun C T and Huang G L 2009 On the negative effective mass density in acoustic metamaterials *Int. J. Eng. Sci.* **47** 610–7
[4] Zhu R, Liu X N, Hu G K, Sun C T and Huang G L 2014 Negative refraction of elastic waves at the deep-subwavelength scale in a single-phase metamaterial *Nat. Commun.* **5** 5510
[5] Yang M and Sheng P 2017 Sound absorption structures: from porous media to acoustic metamaterials *Ann. Rev. Mater. Res.* **47** 83
[6] Sheng P 2017 Optimal sound-absorbing structures *J. Acoust. Soc. Am.* **141** 3575
[7] Cummer S A, Christensen J and Alù A 2016 Controlling sound with acoustic metamaterials *Nat. Rev. Mater.* **1** 16001
[8] Yang Z, Mei J, Yang M, Chan N H and Sheng P 2008 Membrane-type acoustic metamaterial with negative dynamic mass *Phys. Rev. Lett.* **101** 20430
[9] Chen Y Y, Huang G L, Zhou X M, Hu G K and Sun C T 2014 Analytical coupled vibroacoustic modeling of membrane-type acoustic metamaterials: membrane model *J. Acoust. Soc. Am.* **136** 969–79
[10] Popa B I and Cummer S A 2015 Water-based metamaterials: negative refraction of sound *Nat. Mater.* **14** 363–4
[11] Naify C J, Martin T P, Layman C N, Nicholas M, Thangawng A L, Calvo D C and Orris G J 2014 Underwater acoustic omnidirectional absorber *Appl. Phys. Lett.* **104** 073505
[12] Meng H, Wen J H, Zhao H G and Wen X S 2012 Optimization of locally resonant acoustic metamaterials on underwater sound absorption characteristics *J. Sound Vib.* **331** 4406–16
[13] Yu D L, Liu Y Z, Wang G, Zhao H G and Qiu J 2006 Flexural vibration band gaps in Timoshenko beams with locally resonant structures *J. Appl. Phys.* **100** 124901
[14] Xiao Y, Wen J H, Yu D L and Wen X S 2013 Flexural wave propagation in beams with periodically attached vibration absorbers: band-gap behavior and band formation mechanisms *J. Sound Vib.* **332** 867–93
[15] Gao N, Wu J H, Yu L and Xin H 2016 Design of radial phononic crystal using annular soft material with low-frequency resonant elastic structures *Phys. Lett.* A **380** 3326–32
[16] Gao N, Hou H, Wu J H and Cheng B 2016 Low frequency band gaps below 10 Hz in radial flexible elastic metamaterial plate *J. Phys.* D **49** 435501
[17] Tan K T, Huang H H and Sun C T 2014 Blast-wave impact mitigation using negative effective mass density concept of elastic metamaterials *Int. J. Impact Eng.* **64** 20–9
[18] Chen Y Y, Barnhart M V, Chen J K, Hu G K, Sun C T and Huang G L 2016 Dissipative elastic metamaterials for broadband wave mitigation at subwavelength scale *Compos. Struct.* **136** 358–71
[19] Liu X N, Hu G K, Huang G L and Sun C T 2011 An elastic metamaterial with simultaneously negative mass density and bulk modulus *Appl. Phys. Lett.* **98** 251907
[20] Sun H W, Du X W and Pai P F 2010 Theory of metamaterial beams for broadband vibration absorption *J. Intell. Material Syst. Struct.* **21** 1085–101
[21] Xiao Y, Wen J H and Wen X S 2012 Longitudinal wave band gaps in metamaterial-based elastic rods containing multi-degree-of-freedom resonators *New J. Phys.* **14** 033042

[22] Zhu R, Liu X N, Hu G K, Sun C T and Huang G L 2014 A chiral elastic metamaterial beam for broadband vibration suppression *J. Sound Vib.* **333** 2759–73
[23] Chen H, Li X P, Chen Y Y and Huang G L 2017 Wave propagation and absorption of sandwich beams containing interior dissipative multi-resonators *Ultrasonics* **76** 99–108
[24] Colombi A, Roux P, Guenneau S, Gueguen P and Craster Richard V 2016 Forests as a natural seismic metamaterial: rayleigh wave bandgaps induced by local resonances *Sci. Rep.* **6** 19238
[25] Brûlé S, Javelaud E H, Enoch S and Guenneau S 2014 Experiments on seismic metamaterials: molding surface waves *Phys. Rev. Lett.* **112** 133901
[26] Kim S H and Das M P 2012 Seismic waveguide of metamaterials *Mod. Phys. Lett.* B **26** 1250105
[27] Lakes R 2001 Extreme damping in composite materials with a negative stiffness phase *Phys. Rev. Lett.* **86** 2897–900
[28] Lakes R, Lee T, Bersie A and Wang Y C 2001 Extreme damping in composite materials with negative-stiffness inclusions *Nature* **410** 565–7
[29] Klatt T and Haberman M R 2013 A nonlinear negative stiffness metamaterial unit cell and small-on-large multiscale material model *J. Appl. Phys.* **114** 033503
[30] Khajehtourian R and Hussein M 2014 Dispersion characteristics of a nonlinear elastic metamaterial *AIP Adv.* **4** 124308
[31] Zhou W J, Li X P, Wang Y S, Chen W Q and Huang G L 2018 Spectro-spatial analysis of wave packet propagation in nonlinear acoustic metamaterials *J. Sound Vib.* **413** 250–69
[32] Airoldi L and Ruzzene M 2011 Design of tunable acoustic metamaterials through periodic arrays of resonant shunted piezos *New J. Phys.* **13** 113010
[33] Bergamini A, Delpero T, Simoni L D, Lillo L D, Ruzzene M and Ermanni P 2014 Phononic crystal with adaptive connectivity *Adv. Mater.* **26** 1343–7
[34] Chen S B, Wang G, Wen J H and Wen X S 2013 Wave propagation and attenuation in plates with periodic arrays of shunted piezo-patches *J. Sound Vib.* **332** 1520–32
[35] Chen S B, Wen J H, Wang G and Wen X S 2013 Tunable band gaps in acoustic metamaterials with periodic arrays of resonant shunted piezos *Chin. Phys.* B **22** 074301
[36] Zhang H, Wen J H, Xiao Y, Wang G and Wen X S 2015 Sound transmission loss of metamaterial thin plates with periodic subwavelength arrays of shunted piezoelectric patches *J. Sound Vib.* **343** 104–20
[37] Chen Y Y, Huang G L and Sun C T 2014 Band gap control in an active elastic metamaterial with negative capacitance piezoelectric shunting *J. Vib. Acoust.* **136** 061008
[38] de Marneffe B and Preumont A 2008 Vibration damping with negative capacitance shunts: theory and experiment *Smart Mater. Struct.* **17** 035015
[39] Zhou W, Wu Y and Zuo L 2015 Vibration and wave propagation attenuation for metamaterials by periodic piezoelectric arrays with high-order resonant circuit shunts *Smart Mater. Struct.* **24** 65021
[40] Cardella D, Celli P and Gonella S 2016 Manipulating waves by distilling frequencies: a tunable shunt-enabled rainbow trap *Smart Mater. Struct.* **25** 085017
[41] Wang G, Wang J W, Chen S B and Wen J H 2011 Vibration attenuations induced by periodic arrays of piezoelectric patches connected by enhanced resonant shunting circuits *Smart Mater. Struct.* **20** 125019
[42] Wang G and Chen S B 2016 Large low-frequency vibration attenuation induced by arrays of piezoelectric patches shunted with amplifier–resonator feedback circuits *Smart Mater. Struct.* **25** 015004
[43] Wang G, Cheng J Q, Chen J W and He Y Z 2017 Multi-resonant piezoelectric shunting induced by digital controllers for subwavelength elastic wave attenuation in smart metamaterial *Smart Mater. Struct.* **26** 025031
[44] Bergamini A E, Zündel M, Flores Parra E A, Delpero T, Ruzzene M and Ermanni P 2015 Hybrid dispersive media with controllable wave propagation: a new take on smart materials *J. Appl. Phys.* **118** 154310
[45] Chen Y Y, Hu G K and Huang G L 2017 A hybrid elastic metamaterial with negative mass density and tunable bending stiffness *J. Mech. Phys. Solids* **105** 179–98
[46] Zhu R, Chen Y Y, Barnhart M V, Hu G K, Sun C T and Huang G L 2016 Experimental study of an adaptive elastic metamaterial controlled by electric circuits *Appl. Phys. Lett.* **108** 011905
[47] Chen Y Y, Hu G K and Huang G L 2017 An adaptive metamaterial beam with hybrid shunting circuits for extremely broadband control of flexural waves *Smart Mater. Struct.* **25** 105036
[48] Giurgiutiu V 2014 *Structural Health Monitoring with Piezoelectric Wafer Active Sensors* (Columbia, SC: Elsevier)